Rule-Based Time-Optimal Engine-Start Coordination Control With a Predesigned Vehicle Acceleration Trajectory in P2 Hybrid Electric Vehicles

Ziwang Lu

State Key Laboratory of Automotive Safety and Energy School of Vehicle and Mobility, Tsinghua University, Beijing 100084, China e-mail: luzw1992@gmail.com

Guangyu Tian

Professor
State Key Laboratory of Automotive Safety and Energy School of Vehicle and Mobility, Tsinghua University, Beijing 100084, China e-mail: tian_gy@tsinghua.edu.cn

Simona Onori

Professor
Department of Energy Resources Engineering, Stanford University, Stanford, CA 94305 e-mail: sonori@stanford.edu

Removing the integrated starter generator (ISG) in P2 hybrid electric vehicles (HEVs) reduces the overall cost of the powertrain, yet it comes with an additional control complexity of the engine-start process. An appropriate coordination control strategy between the internal combustion engine (ICE), drive motor, and clutch is necessary to reduce the time for the engine-start while constraining the vehicle jerk. A time-optimal coordination control strategy with a predesigned vehicle acceleration trajectory is proposed from results of nonlinear model predictive control (NMPC), which can reduce the time for the engine-start process and obtain a small vehicle jerk. A dynamic model for the engine-start process is first built. In this model, a cylinder-by-cylinder engine model (CCEM) is derived to describe the ICE dynamics. A Karnopp and Stribeck combined wet clutch model is proposed to handle effects of speed difference on the torque, and calculation problem of frequent switches when crossing zero speed point. Subsequently, the optimal control problem is formulated with selected states and solved with NMPC. Finally, a rule-based control strategy is extracted from results of NMPC. Simulation results show that the engine-start process can finish within 260 ms, 13.3% less than the previous study, with a predesigned vehicle acceleration to ensure the vehicle jerk within $10\ m/s^3$ and the peak to peak vehicle acceleration within $0.2\ m/s^2$ in the case study under investigation.
[DOI: 10.1115/1.4056154]

Keywords: hybrid electric vehicle, P2 architecture without ISG, engine-start control, time-optimal control

1 Introduction

Hybrid electric vehicles (HEVs) are massively invading our roads, and have become an important development strategy in many countries to address climate changes concerns [1]. There are two types of HEVs according to the power-split mode, i.e., series or parallel. Parallel HEVs are categorized into P0, P1, P2, P3, and P4 according to the position of the motor in the powertrain [2]. The five configurations are shown in Fig. 1. In this paper, we focus on P2 architecture, which is illustrated in Fig. 2(*a*). The powertrain includes an integrated starter generator (ISG), an internal combustion engine (ICE), a motor, and a clutch in between. The ISG is used to crank the ICE to the idle speed, which reduces the time for the engine-start process. To reduce the cost of the powertrain, the ISG is sometimes removed, shown in Fig. 2(*b*). In this configuration, the engine is started through the coordination control between the ICE, drive motor, and clutch. Removing the ISG brings larger jerks and increases the time duration for the engine-start process, which has a negative effect on the vehicle's drivability.

This study focuses on coordination control between the internal combustion engine, motor, and clutch, aimed at minimizing the engine-start time while reducing jerks. Smith et al. [3] built a dynamic model using Simcenter Amesim, a software tool for modeling, simulation, and dynamic analysis of hydraulic and

mechanical systems. Then they proposed a four-step control strategy, comprising cranking, ignition, preparation, and lockup. At each stage, a compensation torque for the clutch was provided by the motor from the estimated clutch torque. The strategy was validated on a test bench. However, the effect of the speed difference between the input and output plates of the clutch on the clutch torque was disregarded, resulting in neglecting of the ICE torque ripple transmitted to the clutch. To that end, a more precise clutch model considering the influence of speed difference on the clutch friction was built [4], but the ICE was not involved in the speed synchronization process, which resulted in slow synchronization. Kum et al. [5] solved a numerical optimal control problem and
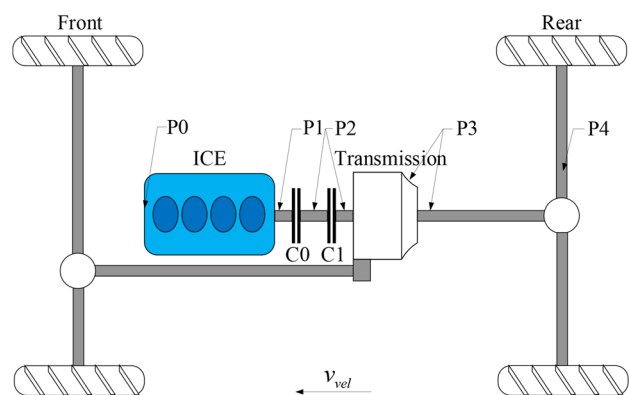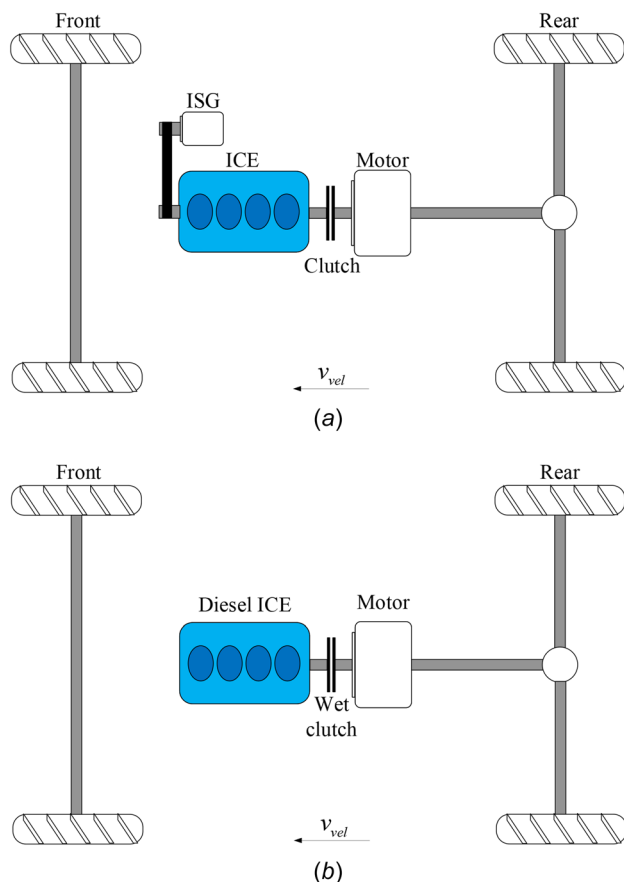

Fig. 1   Different architectures of HEV in parallel

Fig. 2 P2 architecture with or without ISG. (*a*) P2 with ISG and (*b*) P2 without ISG.

found an analytical optimal control law for the engine-start process with a more detailed ICE model reflecting the four-stroke working process, but the ICE torque was not applied to the speed synchronization process either. Chen et al. [6] studied the engine-start process utilizing an ISG and proposed a model reference control strategy to reduce the vehicle jerk. Lei et al. [7] built the powertrain system dynamic model with a dual clutch transmission and made a rule-based coordination control strategy with proportional-integral-differential (PID) controllers accounting for both the gear-shifting process and engine-start process. Xu et al. [8,9] used a pressure to crank angle map to simulate the engine torque and proposed an empirical control strategy for the engine-start process. Ning et al. [10] gave some general rules to start the engine with P2 architecture using a PID controller. Zhao et al. [11,12] built a detailed hybrid electric vehicle simulation model and achieved an efficient and practical control strategy to reduce the fuel consumption during the engine-start process. Cvok et al. [13] also took account of the transmission upshift process and improved the drivability by applying the multi-objective genetic algorithm MOGA-II incorporated within the mode FRONTIER optimization environment. Sun et al. [14] presented a novel single-motor power-reflux architecture and built the corresponding dynamic model and a control strategy. The proposed control strategy could improve the drivability.

Designing an optimal control strategy is the focus of this paper. Model predictive control (MPC) algorithm has been applied by many researchers. A rule-based control strategy derived from the MPC is utilized to the engine-start process to eliminate the power interruption in a hybrid electric vehicle with two motors [15]. Dudek et al. [16] and Stroe et al. [17] developed an energy management strategy based on MPC, obtaining fuel savings of 5%. Han et al. [18] achieved a MPC strategy for a hybrid electric

vehicle with a belted starter alternator. With the belted starter alternator, the diesel engine can start after 300 ms. However, few researchers design an optimal control accounting for the ICE torque.

Besides that, modeling the ICE and clutch [19] is also key to study the drivability of a P2 hybrid electric vehicle. The peak-to-peak vehicle acceleration is always utilized to evaluate the drivability [10,20–23]. There are two main approaches from which we can build an ICE model, either a cylinder-by-cylinder engine model (CCEM) or a mean value engine model (MVEM). A CCEM is built through dynamic cylinder pressure analysis at every crank angle for each cylinder. The MVEM is a more simplified model, in which the pressure is taken to be the mean value of four strokes (720 deg in general) of all cylinders. Karlsson and Fredriksson [24] analyzed the effects of these two engine models on the powertrain control, and claimed that it is not clear that the MVEM is adequate for powertrain control due to the nonlinearity of the clutch. For clutch models, the coulomb friction model is usually used for a dry clutch system. To avoid oscillations during calculation when crossing the zero speed point, Karnopp [25] proposed a small speed area near the zero speed. Stribeck et al. [26,27] proposed a friction model, which is named "Stribeck friction model," to describe the wet clutch friction considering the viscous effect.

As stated above, an ICE model that includes the relationship between the crank angle and engine torque, and a clutch model that accounts for the influence of both the speed difference and pressure on the friction torque are necessary. An online optimal control law to coordinate the clutch, ICE, and drive motor accounting for the ICE torque is desirable.

This paper is organized as follows: first, the mechanical structure of the powertrain is presented. Then, the dynamic model for the engine-start process with a cylinder-by-cylinder diesel engine model and a clutch model combining the Stribeck model and Karnopp model is constructed. Next, a time-optimal control problem considering drivability is formulated and solved with the nonlinear model predictive control (NMPC). Subsequently, referring to the related rule-extraction methods [28,29], a rule-based control strategy is derived with respect to the results of NMPC. Moreover, one engine-start case study and the factors that influence the clutch torque and the lock-up process are analyzed. Finally, concluding remarks are given in the end.

2 Mechanical Structure

The mechanical structure of a P2 powertrain without an ISG is shown in Fig. 2(*b*). The system comprises a diesel engine, a clutch, a drive motor, and a final drive. The ICE is connected to the drive motor through the clutch. There is no transmission, since it is assumed that the gear-shifting process does not occur during the engine-start process.

Parameters of the system are shown in Table 1.

3 P2 Powertrain Dynamic Model

The P2 powertrain dynamic model is first derived, which comprises a cylinder-by-cylinder diesel engine model, a wet clutch model with a combination of a Stribeck and Karnopp friction model, a drive motor model, and a vehicle longitudinal dynamic model. Subsequently, based on these models, the integrated powertrain dynamic model is derived.

Table 1 Parameters of the system

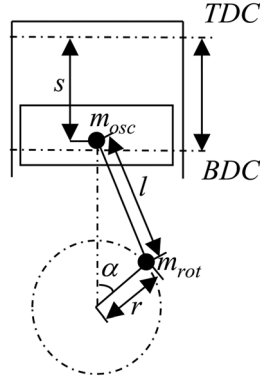| Name	Value	Unit
Diesel engine rated power	85	kW
Electric motor rated power	60	kW
Final drive ratio	4.05	—

Fig. 3   Geometric diagram of one cylinder

3.1   Cylinder-by-Cylinder Diesel Engine Torque Model. In this section, we derive the dynamic model of the ICE based on the Lagrange's equation of motion of the second kind. First, the dynamic model for a single cylinder which we mark j is derived. Then, the dynamic model for four cylinders is obtained by superposition.

3.1.1   Dynamic Model for a Single Cylinder. The geometric diagram of cylinder j is depicted in Fig. 3. Lagrange's equation of motion of the second kind is given by

$$\frac{d}{dt}\left(\frac{\partial L_j}{\partial \dot{\alpha}_j}\right) - \frac{\partial L_j}{\partial \alpha_j} = Q_j \tag{1}$$

where α_j denotes the crank angle, L_j represents the Lagrange function, and Q_j is the external torque.

Furthermore, L_j can be expressed as follows:

$$L_j = T_j - V_j \tag{2}$$

where T_j and V_j represent the kinetic energy and potential energy, respectively. The potential energy in this system is the gravitational potential energy, which can be disregarded compared to the kinetic energy. Therefore, $L_j = T_j$.

To solve the kinetic energy T_j, we divide the mass into two parts, the rotational and oscillational parts. For the oscillational part, a lumped mass (m_{osc}^j) is used to represent the oscillational mass, calculated as follows:

$$m_{osc}^j = m_{piston}^j + m_{rod,osc}^j \tag{3}$$

where m_{piston}^j and $m_{rod,osc}^j$ represent the piston mass and equivalent oscillational mass of the connecting rod, respectively. For simplicity, $m_{rod,osc}^j$ is calculated by regarding the connecting rod as an equivalent massless rod with two balls, as depicted in Fig. 4, hence $m_{rod,osc}^j = m_{rod}^j(l_{osc}^j/l_j)$.

For the rotational part, we use m_{rot}^j to represent the lumped mass, which can be calculated as

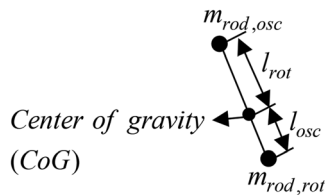$$m_{rot}^j = m_{crank}^j + m_{rod,rot}^j \tag{4}$$

Fig. 4   Equivalent lumped masses of the connecting rod

where m_{crank}^j and $m_{rod,rot}^j$ are the crank mass and equivalent rotational mass of the connecting rod, as depicted in Fig. 4. The equivalent rotational mass of the connecting rod is then solved as $m_{rod,rot}^j = m_{rod}^j(l_{rot}^j/l_j)$.

Finally, the kinetic energy is calculated as follows:

$$T_j = \frac{1}{2}m_{osc}^j \dot{s}_j^2 + \frac{1}{2}m_{rot}^j r_j^2 \dot{\alpha}_j^2 \tag{5}$$

Hence, the Lagrange function is

$$\begin{aligned} L_j = T_j &= \frac{1}{2}m_{osc}^j \dot{s}_j^2 + \frac{1}{2}m_{rot}^j r_j^2 \dot{\alpha}_j^2 \\ &= \frac{1}{2}m_{osc}^j\left(\frac{ds_j}{d\alpha_j}\dot{\alpha}_j\right)^2 + \frac{1}{2}m_{rot}^j r_j^2 \dot{\alpha}_j^2 \\ &= \frac{1}{2}\left(m_{osc}^j\left(\frac{ds_j}{d\alpha_j}\right)^2 + m_{rot}^j r_j^2\right)\dot{\alpha}_j^2 \end{aligned} \tag{6}$$

The external torque Q_j comprises the friction force between the piston and cylinder Q_{fric}, pressure on the piston from the atmosphere Q_{atm}, pressure on the piston from the gas in the cylinder $Q_{cylinder}$, and load Q_{load} on the crank from the vehicle, which can be calculated, respectively, as:

$$\begin{aligned} Q_{fric}^j &= F_{fric}^j \frac{ds_j}{d\alpha_j} = -c_f^j \dot{s}_j \frac{ds_j}{d\alpha_j} \\ &= -c_f^j\left(\frac{ds_j}{d\alpha_j}\dot{\alpha}_j\right)\frac{ds_j}{d\alpha_j} = -c_f^j\left(\frac{ds_j}{d\alpha_j}\right)^2\dot{\alpha}_j \\ Q_{atm}^j &= -P_{atm}A_p^j \frac{ds_j}{d\alpha_j} \\ Q_{cylinder}^j &= T_{cylinder}^j \\ Q_{load}^j &= -T_{load}^j = -\frac{T_{load}}{N_{Cyl}} \end{aligned} \tag{7}$$

where P_{atm} denotes the atmospheric pressure, A_p denotes the piston area, and T_{load} represents the load torque from the vehicle.

The total external torque can be calculated as follows:

$$\begin{aligned} Q_j &= Q_{fric}^j + Q_{atm}^j + Q_{cylinder}^j + Q_{load}^j \\ &= -c_f^j\left(\frac{ds_j}{d\alpha_j}\right)^2\dot{\alpha}_j - P_{atm}A_p^j \frac{ds_j}{d\alpha_j} + T_{cylinder}^j - T_{load}^j \end{aligned} \tag{8}$$

The dynamic model for cylinder j can be derived by substituting the Lagrange function L_j and external force Q_j in Eq. (1) using Eqs. (6) and (8)

$$\begin{aligned} &\left(m_{rot}^j r_j^2 + m_{osc}^j\left(\frac{ds_j}{d\alpha_j}\right)^2\right)\ddot{\alpha}_j + m_{osc}^j \frac{ds_j}{d\alpha_j}\left(\frac{d^2 s_j}{d^2\alpha_j}\right)\dot{\alpha}_j^2 \\ &= c_f^j\left(\frac{ds_j}{d\alpha_j}\right)^2\dot{\alpha}_j - P_{atm}A_p^j \frac{ds_j}{d\alpha_j} + T_{cylinder}^j - T_{load}^j \end{aligned} \tag{9}$$

In Eq. (9), the ICE torque owing to the gas pressure in the cylinder, $T_{cylinder}^j$, needs to be solved. Referring to related researches [30–32], we also divide the ICE torque, $T_{cylinder}^j$, into basic torque, T_{basic}^j, and combustion torque, T_{comb}^j. Basic pressure torque, T_{basic}^j, indicates the torque resulting from the gas pressure in the cylinder without combustion. Combustion torque, T_{comb}^j, is the torque out of combustion.

(a) Basic pressure torque T_{basic}^j

The basic pressure torque can be solved as follows:

$$T_{basic}^j = P_{basic}^j A_p^j \frac{ds_j}{d\alpha_j} \tag{10}$$

where P_{basic}^j can be approximated as follows [30]:

$$P_{\text{basic}}^j = \begin{cases} P_{\text{intake}}^j, & \alpha_j \in [0\,\text{deg}, 180\,\text{deg}] \\ P_{\text{intake}}^j \left(\dfrac{V_{\text{intake}}^j}{V_c^j}\right)^{\gamma}, & \alpha_j \in [180\,\text{deg}, 540\,\text{deg}] \\ P_{\text{exh}}^j, & \alpha_j \in [180\,\text{deg}, 720\,\text{deg}] \end{cases} \quad (11)$$

(b) Combustion torque T_{comb}^j

The torque, T_{comb}^j, owing to combustion can be approximated as follows:

$$T_{\text{comb}}^j = \begin{cases} \dfrac{a_j(\alpha_j - 360)^2}{e^{b_j(\alpha_j - 360)}}, & \alpha_j \in [0\,\text{deg}, 180\,\text{deg}] \\ 0, & \text{else} \end{cases} \quad (12)$$

where $a_j = \frac{4 \times 360 T_{c,\text{hp}}^{\bar{j}}}{(\alpha_{\text{max}j} - 360)^3}$, $b_j = \frac{2}{\alpha_{\text{max}j} - 360}$, and $T_{c,\text{hp}}^{\bar{j}} = \frac{30 \eta_{\text{vol}} Q_{\text{HV}} \dot{m}_f^j}{n_{\text{eng}} \pi}$. α_{max} is 395 deg in this study.

3.1.2 Dynamic Model for Four Cylinders. The dynamic model for the ICE with four cylinders can be derived as follows:

$$\ddot{\alpha} = \frac{\sum\limits_{j=1}^{4}\left(T_{\text{basic}}^j + T_{\text{comb}}^j - T_{\text{fric}}^j - T_{\text{atm}}^j - T_{\text{mass}}^j\right) - T_{\text{load}}}{J_e^{\text{cylinder}}} \quad (13)$$

where α is the crank angle of the ICE, $T_{\text{basic}}^j = P_{\text{basic}}^j A_p^j \frac{ds_j}{d\alpha_j}$, $T_{\text{atm}}^j = P_{\text{atm}} A_p^j \frac{ds_j}{d\alpha_j}$, $T_{\text{fric}}^j = c_f (ds_j/d\alpha_j)^2 \dot{\alpha}$, $T_{\text{mass}}^j = m_{\text{osc}}^j (ds_j/d\alpha_j)(d^2 s_j/\ d^2\alpha_j) \dot{\alpha}_j^2$, and $J_e^{\text{cylinder}} = \sum_{j=1}^{4}(m_{\text{rot}}^j r_j^2 + m_{\text{osc}}^j (ds_j/d\alpha_j)^2)$.

Figure 5 illustrates the ICE torque trajectories with a single cylinder and four cylinders, respectively.

In this paper, we assume emission system has little influence on the ICE torque since the engine-start process takes really little time and the emissions have very small fluctuations according to Ref. [12] especially when the cranking torque is high.

3.2 Clutch Model. To derive the clutch model, the friction coefficient and torsional shocker absorber model are first given. Subsequently, the state transition mechanism between the slipping mode and lock-up mode is resolved. The clutch dynamics are then derived according to the state transition mechanism.

3.2.1 Friction Coefficient. Combining the Karnopp model [25,33] and Stribeck model [26,27], the friction coefficient of a wet clutch can be calculated as follows:

$$\mu_{\text{clt}} = \begin{cases} \text{sign}(\Delta\omega)\mu_s, & \omega_{\text{kar}} \leq 0 \\ \text{sign}(\omega_{\text{kar}})\left(\mu_s + \dfrac{(\mu_s - \mu_v)}{e^{\left(\frac{\omega_{\text{kar}}}{\Delta\omega_s}\right)^{ce}}} + k_v\omega_{\text{kar}}\right), & \text{else} \end{cases} \quad (14)$$
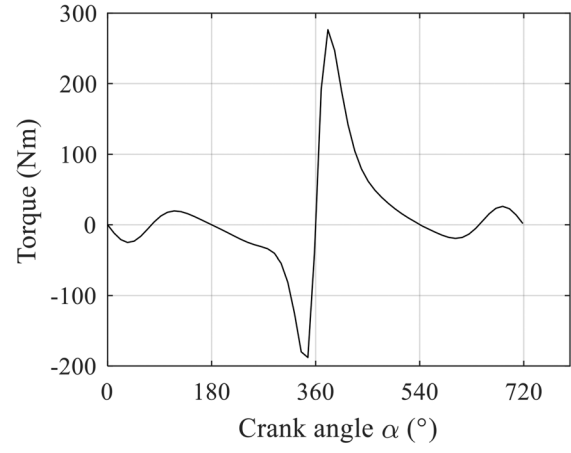
where μ_{clt} is the friction coefficient of the clutch, $\Delta\omega$ denotes the speed difference between the input and output plates of the clutch, μ_s and μ_v is the static and sliding friction coefficients, respectively, $\Delta\omega_s$ is the Stribeck velocity, c_e is the exponent coefficient [34,35], $\omega_{\text{kar}} = |\Delta\omega| - \delta\omega$, $\delta\omega$ is a small speed region set to avoid the calculation problem of frequent switches when crossing zero speed point, shown in Fig. 6, k_v is the linear viscous friction coefficient.

The corresponding curve of the friction coefficient is depicted in Fig. 6.
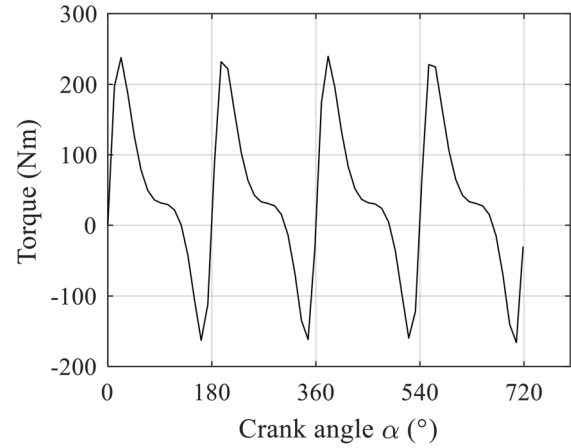
3.2.2 Torsional Shocker Absorber. The torque due to the torsional shocker absorber depends on the relative rotational speed and angle, expressed as follows:

(a)

(b)

Fig. 5 Torque trajectory in one cycle. (*a*) Torque trajectory with a single cylinder. (*b*) Torque trajectory with four cylinders.

Fig. 6 Friction coefficient

$$T_{\text{sd}} = k_\theta \Delta\theta + k_\omega \Delta\omega \quad (15)$$

where T_{sd} denotes the torsional torque; k_θ and k_ω are the stiffness of the spring and coefficient of the damper, and $\Delta\theta$ and $\Delta\omega$ are
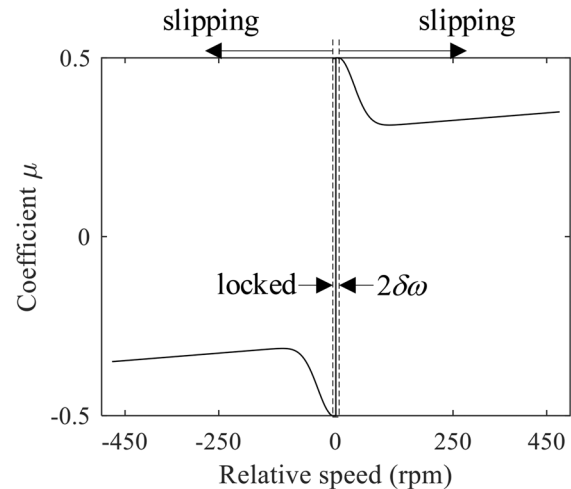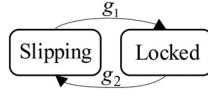
Fig. 7 Status transition logic of the clutch ($g_1 = |T_{\text{clt}}^{\text{stick}}| \le T_{\text{clt}}^{\text{max}}$ and $|\omega_{\text{clt}}^{\text{in}} - \omega_{\text{clt}}^{\text{out}}| \le \delta\omega$, $g_2 = |T_{\text{clt}}^{\text{stick}}| > T_{\text{clt}}^{\text{max}}$)
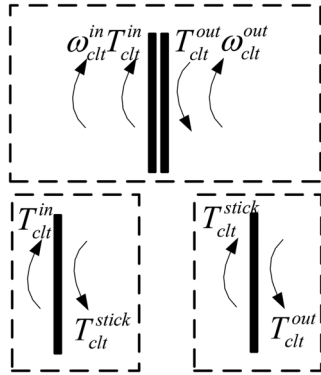
Fig. 8 Force analysis of the clutch

the relative rotational angle and speed between the two ends, respectively.

3.2.3 State Transition Mechanism. The state transition scheme is depicted in Fig. 7. The clutch can be in one of two states, based on whether it is slipping or locked.

To determine the status of the clutch, the stick torque in the locked state first needs to be determined. According to the force analysis in Fig. 8, the stick torque can be calculated as follows:

$$T_{\text{clt}}^{\text{stick}} = \frac{T_{\text{clt}}^{\text{in}} J_{\text{clt}}^{\text{out}} + T_{\text{clt}}^{\text{out}} J_{\text{clt}}^{\text{in}}}{J_{\text{clt}}^{\text{in}} + J_{\text{clt}}^{\text{out}}} \tag{16}$$

3.2.4 Clutch Model. The dynamics of the clutch in each state can be calculated as follows:

(a) Slipping dynamics
The slipping dynamics for the clutch can be categorized into two parts, the input disk of the clutch and output disk of the clutch, expressed as follows:

$$\dot{\omega}_{\text{clt}}^{\text{in}} = \frac{T_{\text{clt}}^{\text{in}} - T_{\text{clt}}}{J_{\text{clt}}^{\text{in}}}$$
$$\dot{\omega}_{\text{clt}}^{\text{out}} = \frac{T_{\text{clt}} - T_{\text{clt}}^{\text{out}}}{J_{\text{clt}}^{\text{out}}} \tag{17}$$

where $T_{\text{clt}} = N_{\text{clt}} \mu_{\text{clt}} p_{\text{clt}} A_{\text{eff}}^{\text{clt}}$.
(b) Locked dynamics
When the clutch is locked, the input disk and output disk have the same dynamics, calculated as follows:

$$\dot{\omega}_{\text{clt}}^{\text{in}} = \dot{\omega}_{\text{clt}}^{\text{out}} = \frac{T_{\text{clt}}^{\text{in}} - T_{\text{clt}}^{\text{out}}}{J_{\text{clt}}^{\text{in}} + J_{\text{clt}}^{\text{out}}} \tag{18}$$

3.3 Drive Motor Model. To simplify the motor dynamics, a first-order inertia model is used, expressed as follows:

$$T_{\text{motor}} = \frac{1}{1 + \tau_m s} T_m^{\text{cmd}}$$
$$\dot{\omega}_{\text{motor}} = \frac{T_{\text{motor}}}{J_{\text{motor}}} \tag{19}$$

where T_{motor} is the drive motor torque; T_m^{cmd} is the drive motor torque command; and τ_m denotes the motor time constant.

3.4 Vehicle Dynamic Model. The resistances from the vehicle include the aerodynamics, rolling resistance, and road slope. The inertia resistance is not included in the vehicle resistance since we want to solve the vehicle acceleration. The vehicle resistance can be calculated as follows:

$$F_{f\_\text{vel}} = F_w + F_f + F_i$$
$$= \frac{\rho C_D A}{2} v_{\text{vel}}^2 + \mu_f mg \cos(\beta) + mg \sin(\beta) \tag{20}$$

where F_w, F_f, and F_i represent forces from the aerodynamics, rolling resistance and road slope, respectively. ρ is the air density, C_D is the aerodynamic coefficient, and A is the windward area.

3.5 System Dynamics. The powertrain system's force diagram is shown in Fig. 9(*a*). To better analyze the system dynamics, we divide the system into three parts: Part I includes the ICE and input plate of the clutch, Part II includes the output plate of the clutch, and Part III includes the remaining components connected to the torsional shocker absorber. Accordingly, the forces acting on the powertrain components in the three parts are depicted in Figs. 9(*b*)–9(*d*). Then rotational angles and speeds of the three parts can be derived as

$$\begin{cases} \dot{\theta}_1 = \omega_1 \\ \dot{\theta}_2 = \omega_2 \\ \dot{\theta}_3 = \omega_3 \\ \dot{\omega}_1 = \dfrac{T_{\text{eng}} - T_{\text{clt}}}{J_1} \\ \dot{\omega}_2 = \dfrac{T_{\text{clt}}' - T_{\text{sd}}}{J_2} \\ \dot{\omega}_3 = \dfrac{T_{\text{sd}}' + T_{\text{motor}} - T_{f\_\text{vel}}/i_0}{J_3} \end{cases} \tag{21}$$

where $T_{\text{eng}} = \sum_{j=1}^{4} (T_{\text{basic}}^j + T_{\text{comb}}^j - T_{\text{fric}}^j - T_{\text{atm}}^j - T_{\text{mass}}^j)$, $T_{\text{clt}} = N_{\text{clt}} \mu_{\text{clt}} p_{\text{clt}} A_{\text{eff}}^{\text{clt}}$, $J_1 = J_e^{\text{cylinder}} + J_{\text{in}}^{\text{clt}}$, $T_{\text{clt}} = T_{\text{clt}}'$, $J_3 = \frac{\delta m r_{\text{vel}}^2}{i_0^2} + J_{\text{motor}}$, $J_{\text{in}}^{\text{clt}}$ denotes the input inertia of the clutch, and i_0 denotes the final drive ratio.

3.5.1 State-Space Equations. To solve the optimal coordination control law, we rewrite Eq. (21) using state-space
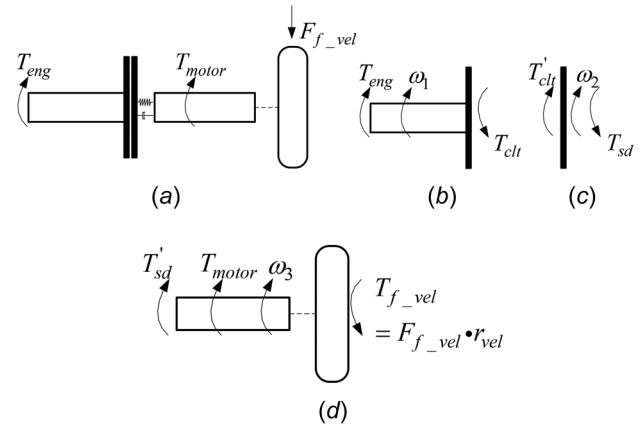
Fig. 9 Diagram of system forces. (*a*) Force analysis of the system. (*b*) Force analysis of part I. (*c*) Force analysis of part II. (*d*) Force analysis of part III.

representation. According to the clutch status shown in Fig. 7, the powertrain status can also be in slipping mode or locked mode. The corresponding stick torque of the clutch can be solved by setting $\dot{\omega}_1 = \dot{\omega}_2$ in Eq. (21), expressed as follows:

$$T_{\text{stick}} = \frac{T_{\text{eng}}J_2 + T_{\text{sd}}J_1}{J_1 + J_2} \tag{22}$$

The system dynamics can then be expressed as follows:

(a) Slipping mode

$$\begin{bmatrix} \dot{\theta}_1 \\ \dot{\theta}_2 \\ \dot{\theta}_3 \\ \dot{\omega}_1 \\ \dot{\omega}_2 \\ \dot{\omega}_3 \end{bmatrix} = \mathbf{f_1}\left(\theta_1, \theta_2, \theta_3, \omega_1, \omega_2, \omega_3, m_f, p_{\text{clt}}, T_m^{\text{cmd}}\right)$$

$$= \begin{bmatrix} \omega_1 \\ \omega_2 \\ \omega_3 \\ \dfrac{f_{T_{\text{eng}}}(\theta_1, \omega_1, m_f) - f_{T_{\text{clt}}}(\omega_1, \omega_2, p_{clt})}{J_1} \\ \dfrac{k_\theta(-\theta_2 + \theta_3) + k_\omega(-\omega_2 + \omega_3) + f_{T_{\text{clt}}}(\omega_1, \omega_2, p_{clt})}{J_2} \\ \dfrac{k_\theta(\theta_2 - \theta_3) + k_\omega(\omega_2 - \omega_3) - f_{T_{f\_\text{vel}}}(\omega_3)/i_0 + f_{T_{\text{motor}}}(T_m^{\text{cmd}})}{J_3} \end{bmatrix} \tag{23}$$

where $f_{T_{f\_\text{vel}}} = F_{f\_\text{vel}}r_{\text{vel}}$, $f_{T_{\text{eng}}} = T_{\text{eng}}$, $f_{T_{\text{clt}}} = T_{\text{clt}}$ in Eq. (21), and $f_{T_{\text{motor}}} = T_{\text{motor}}$ in Eq. (19)

(b) Locked mode

$$\begin{bmatrix} \dot{\theta}_1 \\ \dot{\theta}_2 \\ \dot{\theta}_3 \\ \dot{\omega}_1 \\ \dot{\omega}_2 \\ \dot{\omega}_3 \end{bmatrix} = \mathbf{f_2}\left(\theta_1, \theta_2, \theta_3, \omega_1, \omega_2, \omega_3, m_f, T_m^{\text{cmd}}\right)$$

$$= \begin{bmatrix} \omega_1 \\ \omega_2 \\ \omega_3 \\ \dfrac{k_\theta(-\theta_2 + \theta_3) + k_\omega(-\omega_2 + \omega_3) + f_{T_{\text{eng}}}(\theta_1, \omega_1, m_f)}{J_1 + J_2} \\ \dfrac{k_\theta(-\theta_2 + \theta_3) + k_\omega(-\omega_2 + \omega_3) + f_{T_{\text{eng}}}(\theta_1, \omega_1, m_f)}{J_1 + J_2} \\ \dfrac{k_\theta(\theta_2 - \theta_3) + k_\omega(\omega_2 - \omega_3) - f_{T_{f\_\text{vel}}}(\omega_3)/i_0 + f_{T_{\text{motor}}}(T_m^{\text{cmd}})}{J_3} \end{bmatrix} \tag{24}$$

4 Problem Formulation

The optimal control problem is formulated as follows: First, states are selected to satisfy the Markov property. Subsequently, the control inputs, cost function, and constraints are given.

4.1 State Selection. There are six states (θ_i, ω_i, $i = 1, 2, 3$) in the above dynamic model. To satisfy the requirement of no aftereffect (Markov property) when adopting NMPC algorithm, the motor torque T_{motor} should also be added as another state. Thus, there are seven states in total. However, to achieve the goal of starting the engine, only six states are needed because not all angle states are (ω_i, $i = 1$, 2, 3) necessarily to be solved.

The speed difference ($\Delta\omega_{12} = \omega_1 - \omega_2$) between the engine and input plate of the clutch must be selected because it needs to be decreased to zero to eliminate the jerking motion. T_{eng} is a function of the rotational speed (ω_1) and angle (θ_1) of the engine, T_{clt} is a

function of the clutch pressure (p_{clt}) and the relative rotational speed ($\Delta\omega_{12}$) of the input and output plates of the clutch, T_{sd} is a function of the relative rotational speed ($\Delta\omega_{23} = \omega_2 - \omega_3$) and angle ($\Delta\theta_{23} = \theta_2 - \theta_3$), and T_{f_vel} is a function of the rotational speed (ω_3)

of the vehicle wheel. Hence, θ_1, $\Delta\theta_{23}$, ω_1, $\Delta\omega_{12}$, ω_3, and T_{motor} are necessarily solved. Thus, the dynamic model is stated as follows:

(a) Slipping mode

$$
\begin{bmatrix} \dot{T}_{motor} \\ \dot{\theta}_1 \\ \Delta\dot{\theta}_{23} \\ \dot{\omega}_1 \\ \Delta\dot{\omega}_{12} \\ \dot{\omega}_3 \end{bmatrix} = \mathbf{f_{1r}}\left(T_{motor}, \theta_1, \Delta\theta_{23}, \omega_1, \Delta\omega_{12}, \omega_3, T_m^{cmd}, m_f, p_{clt}\right)
$$

$$
= \begin{bmatrix} \dfrac{1}{\tau_m}\left(-T_{motor} + T_m^{cmd}\right) \\[2mm] \omega_1 \\[2mm] \omega_1 - \Delta\omega_{12} - \omega_3 \\[2mm] \dfrac{1}{J_1}\left(f_{T_{eng}}\left(\theta_1, \omega_1, m_f\right) - f'_{T_{clt}}(\Delta\omega_{12}, p_{clt})\right) \\[2mm] \dfrac{k_\theta\Delta\theta_{23} + k_\omega(\omega_1 - \Delta\omega_{12} - \omega_3) - f'_{T_{clt}}(\Delta\omega_{12}, p_{clt})}{J_2} - \dfrac{f'_{T_{clt}}(\Delta\omega_{12}, p_{clt})}{J_1} \\[2mm] \dfrac{T_{motor} + k_\theta\Delta\theta_{23} + k_\omega(\omega_1 - \Delta\omega_{12} - \omega_3) - f_{T_{f\_vel}}(\omega_3)/i_0}{J_3} \end{bmatrix}
\tag{25}
$$

where $f'_{T_{clt}}(\Delta\omega_{12}, p_{clt}) = T_{clt}$ in Eq. (21).

(b) Locked mode

$$
\begin{bmatrix} \dot{T}_{motor} \\ \dot{\theta}_1 \\ \Delta\dot{\theta}_{23} \\ \dot{\omega}_1 \\ \Delta\dot{\omega}_{12} \\ \dot{\omega}_3 \end{bmatrix} = \mathbf{f_{2r}}\left(T_{motor}, \theta_1, \Delta\theta_{23}, \omega_1, \Delta\omega_{12}, \omega_3, T_m^{cmd}, m_f\right)
$$

$$
= \begin{bmatrix} \dfrac{1}{\tau_m}\left(-T_{motor} + T_m^{cmd}\right) \\[2mm] \omega_1 \\[2mm] \omega_1 - \Delta\omega_{12} - \omega_3 \\[2mm] \dfrac{-k_\theta\Delta\theta_{23} - k_\omega(\omega_1 - \Delta\omega_{12} - \omega_3) + f_{T_{clt}}'(\Delta\omega_{12}, p_{clt})}{J_1 + J_2} \\[2mm] 0 \\[2mm] \dfrac{T_{motor} + k_\theta\Delta\theta_{23} + k_\omega(\omega_1 - \Delta\omega_{12} - \omega_3) - f_{T_{f\_vel}}(\omega_3)/i_0}{J_3} \end{bmatrix}
\tag{26}
$$

4.2 Control Inputs. There are three control inputs: fuel mass, m_f, clutch pressure, p_{clt}, and motor torque command, T_{motor}.

4.3 Cost Function. We wanted to minimize the engine-start time with proper drivability. Therefore, the cost function chosen is

$$
J = \int_0^{t_f} 1 \, dt
\tag{27}
$$

Beyond reducing the engine-start time, drivability is also our concern to decrease the vehicle acceleration vibration. We use the peak to peak vehicle acceleration (also called "acceleration vibration") to reflect the drivability [10,20–23]. It is enhanced by means of proper constraints, shown in Eq. (31).

4.4 Constraints

(a) Dynamic model
    The optimal control problem should be constrained by the system dynamic model, which is presented above.
(b) State constraints

$$
\begin{aligned}
T_{motor} &\in [-T_m^{max}, T_m^{max}] \\
\theta_1 &\in [0, 4\pi] \\
\Delta\theta_{23} &\in [0, 2\pi] \\
\omega_1 &\in [-\omega_1^{max}, \omega_1^{max}] \\
\Delta\omega_{12} &\in [-\Delta\omega_{12}^{max}, \Delta\omega_{12}^{max}] \\
\omega_3 &\in [-\omega_3^{max}, \omega_3^{max}]
\end{aligned}
\tag{28}
$$

(c) Control input constraints

$$m_f = [0, m_f^{\max}]$$
$$p_{\text{clt}} = [0, p_{clt}^{\max}] \tag{29}$$
$$T_m^{\text{cmd}} = [-T_m^{\max}, T_m^{\max}]$$

(d) Terminal constraints

$$|\Delta\omega_{12}| \leq |\delta\omega|$$
$$\text{Clutch mode} = \text{Locked} \tag{30}$$

(e) Drivability constraints
    To ensure drivability, we use peak-to-peak vehicle acceler-ation [22,36] to limit the vehicle acceleration. The peak-to-peak vehicle acceleration is set at 0.4 m/s^2. Therefore, the vehicle acceleration is constrained as follows:

$$a_{\text{vel}} \in [a_{\text{vel}}^{\min}, a_{\text{vel}}^{\max}] \tag{31}$$

where $a_{\text{vel}}^{\min} = a_{\text{vel}}^0 - 0.2$, $a_{\text{vel}}^{\max} = a_{\text{vel}}^0 + 0.2$, a_{vel}^0 is the vehicle acceleration at the beginning of the engine-start process.

The values of parameters above herein are specified in Table 2, where $\omega_1^{\max}$, $\Delta\omega_{12}^{\max}$, and $\omega_3^{\max}$ are achieved by estimating the pos-sible values during the engine-start process.

5 Solution With NMPC

The dynamic model presented in the above state-space form is nonlinear due to T_{eng}, T_{clt}, and T_{f_vel}, which are nonlinear func-tions of the states. To solve this nonlinear time-optimal control problem, NMPC is adopted. NMPC is a receding horizon optimi-zation algorithm, utilized to solve nonlinear optimal control prob-lems to achieve a suboptimal solution. Solving NMPC strategy in real-time is computationally prohibitive though. Yet, the solution from NMPC can be used to generate a rule-based strategy, which is implementable on-board.

The control action can be divided into two stages according to whether the ICE torque is involved. In the first stage, the cranking ICE stage, only the drive motor and clutch are involved, whereas in the second stage, the ICE is involved.

5.1 Cranking ICE. During the cranking ICE process, we want the engine-start process to be completed as soon as possible. Moreover, to solve the nonlinear optimal control problem easier, a quadratic cost function is proposed. To that end, we use the cost function below to replace that in Eq. (27)

$$J_1 = \sum_{k=1}^{N} (\omega_1^k - \omega_s)^2 \tag{32}$$

where ω_s denotes the engine-start speed. If Eq. (32) is minimized, the time duration of the cranking process would also be minimized.

Table 2 Parameters of controller constraints

Name	Value	Unit
$T_m^{\max}$	400	N·m
$\omega_1^{\max}$	200	rad/s
$\Delta\omega_{12}^{\max}$	200	rad/s
$\omega_3^{\max}$	200	rad/s
$m_f^{\max}$	7.5	mg
$p_{\text{clt}}^{\max}$	1000	kPa
δ_ω	2	rad/s
$a_{\text{vel}}^{\max}$	1.0587	m/s^2
$a_{\text{vel}}^{\min}$	0.6587	m/s^2

5.2 Starting ICE. The difference between the starting pro-cess and cranking process is whether the ICE torque is involved. During the starting process, another control input, i.e., the mass of fuel injection m_f, is added. Overall, there are three control inputs during the starting ICE process: the mass of fuel injection m_f, clutch pressure p_{clt}, and motor torque command T_{motor}.

We expect the nonlinear control problem to be easily solved with NMPC. The cost function is replaced by a quadratic function, expressed as follows:

$$J_2 = \sum_{k=1}^{N} (\Delta\omega_{12}^k)^2 \tag{33}$$

If Eq. (33) is minimized, the time duration of the engine-start pro-cess is also minimized. Furthermore, minimizing the cost function would lead $\Delta\omega_{12}$ to reach zero.

5.3 Implementation of NMPC. Both the cranking ICE pro-cess and starting ICE process were solved using NMPC from the Model Predictive Control Toolbox of Matlab [37] with SQP solver [38]. The vehicle acceleration ($a_{\text{vel}} = \dot{\omega}_3 r_{\text{vel}}$) is solved and constrained to the drivability requirements of Eq. (31) when solv-ing the problem with NMPC. We choose five steps as the predic-tion horizon of 1 ms length. The control horizon length is the same as the prediction horizon. The results are shown in Fig. 10.

6 Rule-Based Control Strategies

To obtain a practical control strategy, we first analyzed the results from NMPC, from which a rule-based control strategy was proposed. Finally, a flowchart is derived to show the rule-based control strategy.

6.1 Analysis of Results With NMPC. Figure 10 illustrates the trajectories of states and control inputs during one engine-start
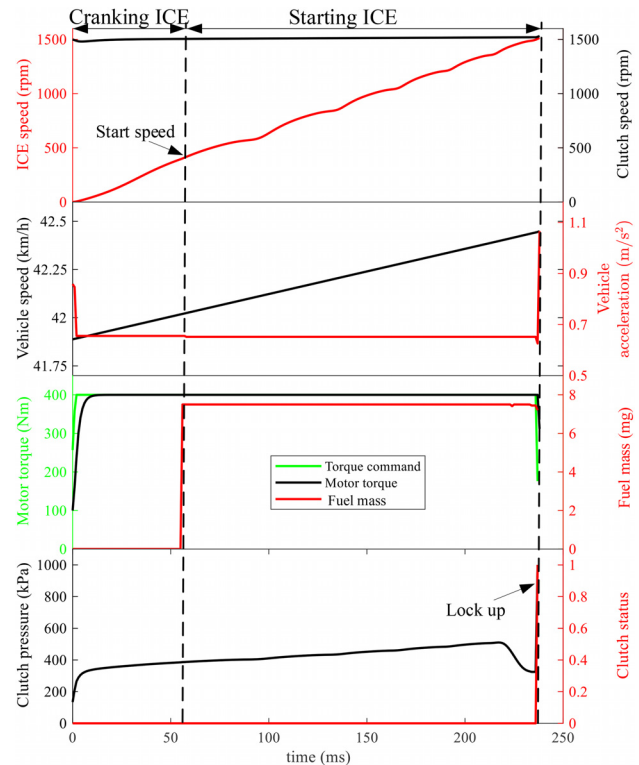
Fig. 10 Trajectories of ICE speed, motor speed, vehicle speed, vehicle acceleration, motor torque, fuel mass, clutch pressure, and clutch status with NMPC
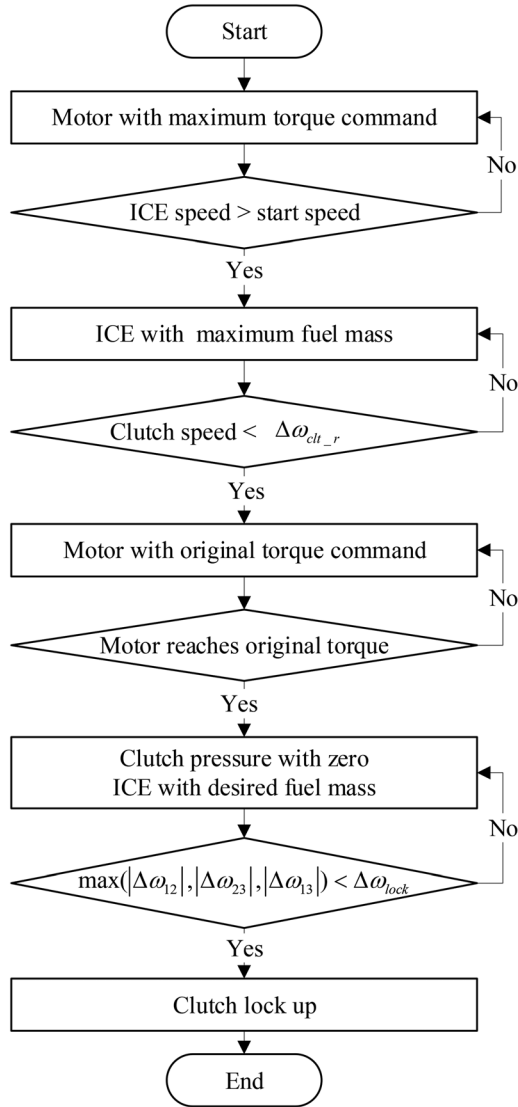
Fig. 11 Rule-based control flowchart

Fig. 12 Trajectories of vehicle acceleration, motor torque, and ICE fuel mass with NMPC with different initial drive shaft speeds

process from the NMPC solution. As depicted, the ICE speed gradually catches up with the clutch speed. The clutch is finally locked up. Simultaneously, the vehicle acceleration is within the drivability constraints. Therefore, NMPC satisfies the control requirements. However, the solution of the NMPC is always not a straightforward solution and not obtained in real-time. To obtain an applicable control strategy, we extract useful information from the results of the NMPC in the form of the rule-based strategy for the real-time implementation.

As depicted in Fig. 10, before the lock-up process, the vehicle acceleration first declines to the minimum with respect to the drivability constraint, and then stays of the minimum. Regarding the control inputs, the ICE injected the maximum mass of fuel after it reached the starting speed, 400 rpm in this case. The motor torque rose to the maximum immediately at the beginning of cranking the ICE. It is reasonable that both the fuel injection and motor torque would rise to their maxima, since we aimed to reduce the time duration. For the lock-up process, a thorough analysis is carried out in Sec. 6.2.2.

We propose a rule-based control strategy summarized as a flow-chart in Fig. 11. The engine-start process can be divided into two processes, the cranking process and starting process. During the cranking process, only the motor and clutch are involved. The motor receives the maximum torque command to crank the ICE. After the ICE speed reaches the start speed, it enters the starting
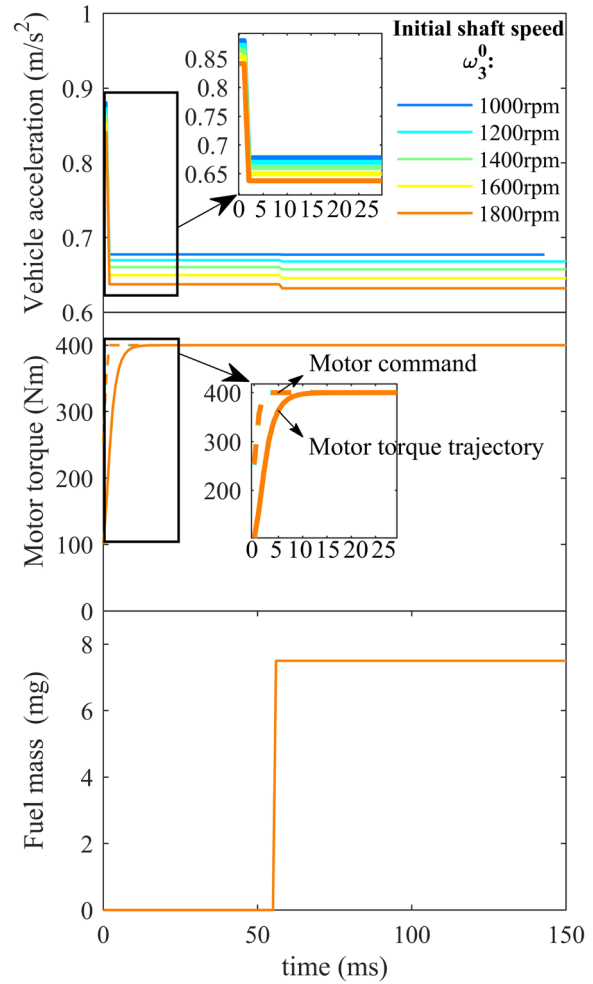
ICE process. This process can be divided into three stages, speed synchronization, recovery, and lockup. At the speed synchronization stage, the ICE runs with maximum mass of fuel injection, the motor operates with maximum torque, the clutch gets the appropriate pressure to keep the vehicle acceleration. At the recovery stage, the motor recovers to its original state, the ICE runs with the desired mass of fuel injection. The clutch pressure decreases slowly to make the vehicle acceleration rise to its original level with the designed slop rate to constrain the vehicle jerk. At the lock-up stage, the motor and ICE keep previous operation states. The clutch first runs with the reasonable pressure to keep the vehicle acceleration and then operates with the maximum pressure to be locked up when the speeds of the ICE, the clutch and drive shaft meet the threshold.

6.2 Extraction of the Rule-Based Control Strategy. A rule-based control strategy is proposed in this section. First, we derived the rule-based control strategy for the cranking ICE and speed synchronization process with respect to the results of NMPC. Then, to achieve better drivability, the lock-up process is studied in detail.

6.2.1 Cranking ICE and Speed Synchronization. According to the analysis in Sec. 6.1, the rules are summarized as follows: (1) the vehicle acceleration first decreases to the minimum and then maintains the minimum; (2) the motor torque rises to the maximum immediately, and then maintains the maximum; and (3) the ICE injects the maximum mass of fuel after the ICE-start speed.

To further validate this, several vehicle acceleration trajectories, motor torque trajectories, and ICE fuel mass trajectories with NMPC with different initial drive shaft speeds are depicted in Fig. 12.

We first design the vehicle acceleration, motor command, and fuel mass trajectories. The vehicle acceleration is designed to constrain the vehicle jerk as follows:

$$a_{\text{vel}} = \begin{cases} a_{\text{vel}}^0 + \dfrac{a_{\text{vel}}^{\text{aim}} - a_{\text{vel}}^0}{\tau_a} t, & t \le \tau_a \\ a_{\text{vel}}^{\text{aim}}, & \text{else} \end{cases} \tag{34}$$

where $a_{\text{vel}}^{\text{aim}}$ is the goal of the vehicle acceleration, $a_{\text{vel}}^{\text{aim}} = a_{\text{vel}}^{\text{min}}$ in this case. τ_a is the time constant, which determines the decline rate of the vehicle acceleration.

The decline rate of the vehicle acceleration means the rate of a_{vel} going down to $a_{\text{vel}}^{\text{aim}}$, which can reflect how fast the vehicle acceleration declines to $a_{\text{vel}}^{\text{aim}}$. To ensure drivability, we constrained the decline rate to $(a_{\text{vel}}^{\text{aim}} - a_{\text{vel}}^0 / \tau_a) \le j_{\text{vel}}$, where j_{vel} represents the vehicle jerk.

The motor command and fuel mass can easily be derived as follows:

$$\begin{aligned} T_m^{\text{cmd}} &= T_m^{\text{max}} \\ m_f &= \begin{cases} 0, & \omega_1 \le \omega_s \\ m_f^{\text{max}}, & \text{else} \end{cases} \end{aligned} \tag{35}$$

The designed vehicle acceleration, motor command, and fuel mass are depicted in Fig. 13.

After designing the trajectories of the vehicle acceleration, motor torque command, and fuel mass, the clutch pressure is resolved following the diagram illustrated in Fig. 14.
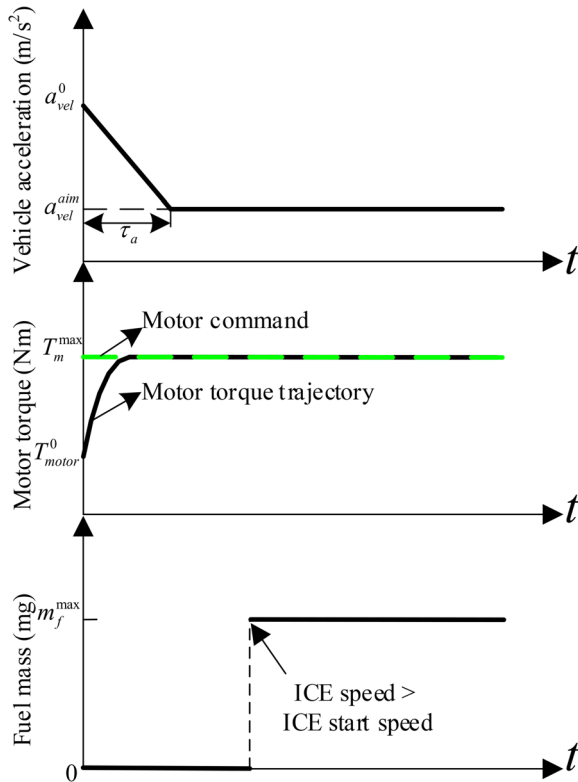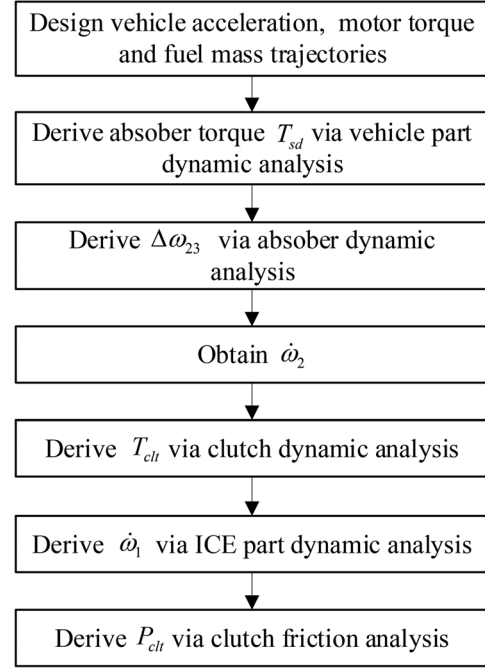

Fig. 14 Diagram of clutch pressure derivation

According to the system dynamics in Eq. (21), the absorber torque is derived as follows:

$$T_{\text{sd}} = J_3 \dot{\omega}_3 + \frac{T_{f\_\text{vel}}}{i_o} - T_{\text{motor}} \tag{36}$$

where $\dot{\omega}_3$ depends on the vehicle acceleration. It is derived as $\dot{\omega}_3 = (a_{\text{vel}}/r_{\text{vel}})i_0$. Motor torque T_{motor} is determined by the torque command T_m^{cmd} according to Eq. (19). It is solved as $T_{\text{motor}} = T_{\text{motor}}^0 + (T_m^{\text{cmd}} - T_{\text{motor}}^0) \cdot (1 - e^{-\frac{t}{\tau_m}})$.

According to the absorber torque in Eq. (15), T_{sd} is derived as follows:

$$T_{\text{sd}} = k_\theta \Delta\theta_{23} + k_\omega \Delta\omega_{23} \tag{37}$$

The first derivative of Eq. (37) is

$$\dot{T}_{\text{sd}} = k_\theta \Delta\omega_{23} + k_\omega \Delta\dot{\omega}_{23} \tag{38}$$

Equation (38) is the first-order linear ordinary differential equation of $\Delta\omega_{23}$. With the resolved T_{sd} in Eq. (36), $\Delta\omega_{23}$ could be obtained by solving the ordinary differential equation in Eq. (38).

Then, $\dot{\omega}_2$ is solved as follows:

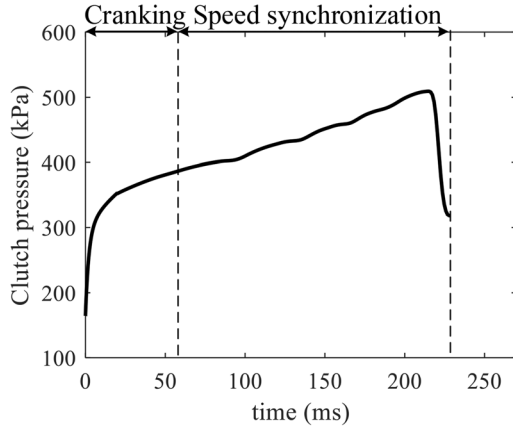$$\dot{\omega}_2 = \dot{\omega}_3 + \Delta\dot{\omega}_{23} \tag{39}$$

Thus, the clutch torque is derived according to Eq. (21).

$$T_{\text{clt}} = T_{\text{sd}} + J_2 \dot{\omega}_2 \tag{40}$$

Based on Eqs. (36), (38), (39), and (40), the clutch torque is derived as follows:

$$\begin{aligned} T_{\text{clt}} = (J_2 + J_3) &\frac{a_{\text{vel}}}{r_{\text{vel}}} i_0 + \frac{T_{f\_\text{vel}}}{i_o} - T_{\text{motor}} \\ &+ J_2 \left(\frac{C_1 k_a + C_2 v_{\text{vel}} a_{\text{vel}} - \dot{T}_{\text{motor}} - k_\theta \Delta\omega_{23}}{k_\omega} \right) \end{aligned} \tag{41}$$

where $C_1 = (i_0 J_3 / r_{\text{vel}})$, $C_2 = (\rho C_D A r_{\text{vel}} / i_o)$.

Fig. 13 Designed trajectories during cranking and speed synchronization process

Fig. 15 Clutch pressure trajectory during cranking and speed synchronization process

We have therefore obtained the clutch torque T_{clt} and speed ω_2 of the output plate of the clutch. To achieve the clutch pressure, we solve for the speed ω_1 of the input plate of the clutch, which equals the ICE speed by integrating $\dot{\omega}_1$ in Eq. (21). Finally, the clutch pressure p_{clt} is solved as

$$p_{clt} = \frac{T_{clt}}{N_{clt}\mu_{clt}A_{eff}^{clt}} \qquad (42)$$

where μ_{clt} is a function of $\Delta\omega_{12} = \omega_1 - \omega_2$ presented in Eq. (14).

The resolved clutch pressure p_{clt} is plotted in Fig. 15.

6.2.2 Lock Up. To obtain better drivability during the lock-up process, we first derive the vehicle acceleration according to the system dynamics in Eq. (21)

$$a_{vel} = \frac{r_{vel}}{J_3 i_o}\left(T_{sd} + T_{motor} - \frac{T_{f\_vel}}{i_o}\right) \qquad (43)$$

According to Eq. (43), the vehicle acceleration depends on the absorber torque, motor torque, and vehicle resistance. The vehicle resistance T_{f_vel} does not change much since it relies on the vehicle speed, and the vehicle speed does not undergo any abrupt change. The motor torque T_{motor} depends on the motor command T_m^{cmd}. The motor command does not change during the lock-up process. Hence, the change of the acceleration mainly depends on the change of the absorber torque.

According to Eq. (37), the absorber torque depends on the absorber speed ($\Delta\omega_{23}$) and absorber angle ($\Delta\theta_{23}$). The absorber speed may undergo an abrupt change during the lock-up process, which would result in a jerk. This is the reason for the bump at the end of the process with NMPC. Figure 16 shows the absorber speed trajectory with the NMPC. Notably, there is a sudden change of the absorber speed, which leads to the vehicle acceleration jerk at the lock-up point, depicted in Fig. 10.

To reduce the vehicle acceleration jerk during the lock-up process, the speed difference between the ICE and output plate of the clutch $\Delta\omega_{12}$, the speed difference between the output plate of the clutch and drive shaft $\Delta\omega_{23}$, the speed difference between the ICE and drive shaft $\Delta\omega_{13}$ needed to be constrained before being locked up, i.e., $\max(|\Delta\omega_{12}|, |\Delta\omega_{23}|, |\Delta\omega_{13}|) < \Delta\omega_{lock}$. To avoid the jerk during the lock-up process, we also analyzed the absorber dynamics after being locked up, expressed as follows:

$$\Delta\dot{\omega}_{23} = \frac{J_3 T_{eng} - (J_1 + J_2)T_{motor}}{J_3(J_1 + J_2)} - \frac{T_{sd}}{J_1 + J_2} - \frac{T_{sd} - T_{f\_vel}}{J_3} \qquad (44)$$

The change of absorber speed also depends on the integration of Eq. (44) besides the abrupt change during the lock up process.
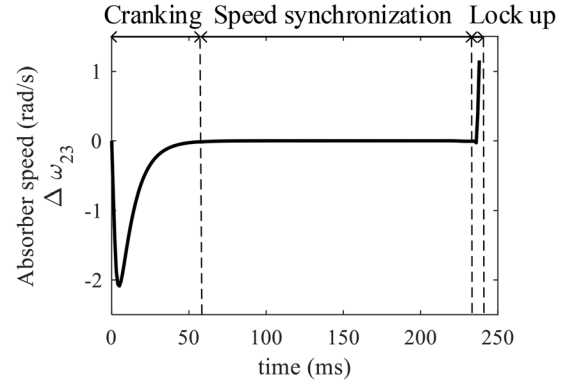
Fig. 16 Absorber speed trajectory with NMPC

Therefore, $\Delta\dot{\omega}_{23}$ should not be significantly large. Thus, before the lock-up process, a recovery process is added. During the recovery process, the fuel mass recovered to their desired values. The motor torque declines to its original level. The vehicle acceleration recovered to its original value with the designed slope rate. The designed trajectories are illustrated in Fig. 17.

The derivation of the clutch pressure is similar to Sec. 6.2.1, shown in Fig. 14. The corresponding clutch pressure trajectory is shown in Fig. 18. As depicted, the clutch pressure declines slowly to keep the vehicle acceleration to be prepared for the lock-up process. At the end of the lock-up process, the clutch pressure rises to the maximum.

7 Results and Analysis

A comparative study between the rule-based strategy and NMPC is first conducted based on one engine-start case to show the feasibility and advantages of the rule-based control strategy. Subsequently, the clutch behavior is further analyzed to explain
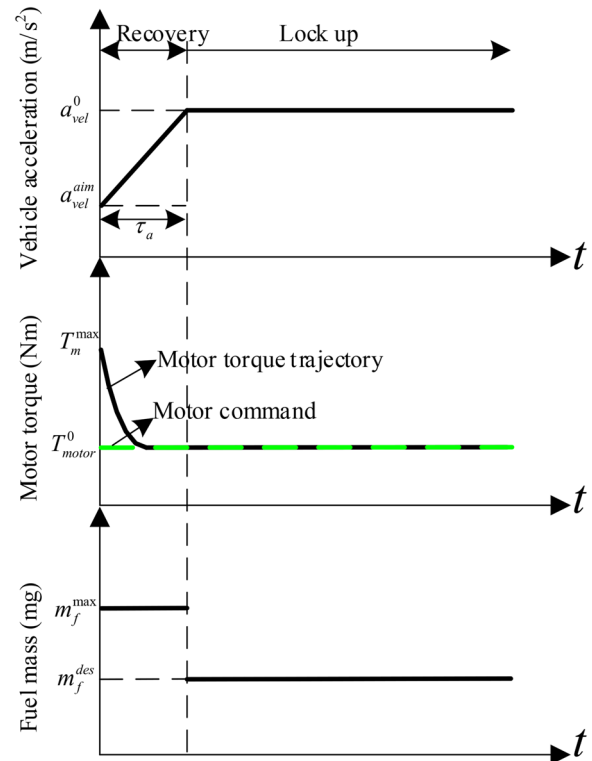
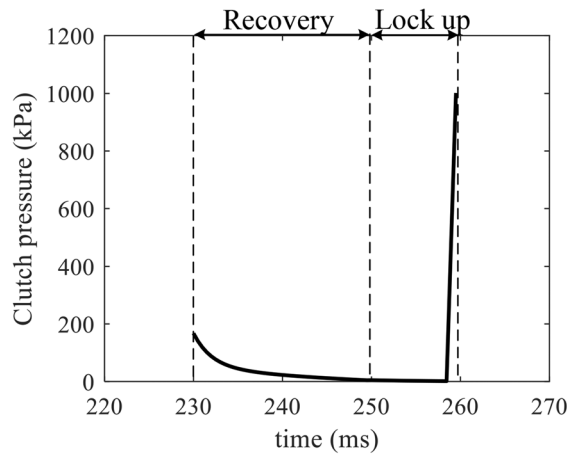**Fig. 17 Designed trajectories during recovery and lock-up processes**

Fig. 18 Clutch pressure trajectory during recovery and lock-up processes

reasons for the time optimality of the control strategy. Moreover, the initial clutch torque at the kissing point is analyzed to high-light the importance of the absorber. The effects of the viscous coefficient and spring stiffness coefficient of the absorber on the initial clutch torque were also analyzed. Finally, the analysis of how to avoid large vehicle jerks during the lock-up process is discussed.

7.1 Comparative Study. Figure 19 illustrates the results with the rule-based control strategy. During the cranking stage, the vehicle acceleration slowed down to the minimum with the designed decline rate. The motor with the maximum torque command aimed to speed up this process. After the ICE speed exceeded the start speed, the ICE started with maximum fuel mass. Before the lock-up process, the mass of fuel injection and motor torque recovered to the desired value and original value, respectively. The clutch operated with appropriate pressure to keep the vehicle acceleration. Then, when the speed difference between the ICE and drive shaft entered the desired range, the clutch locked up.
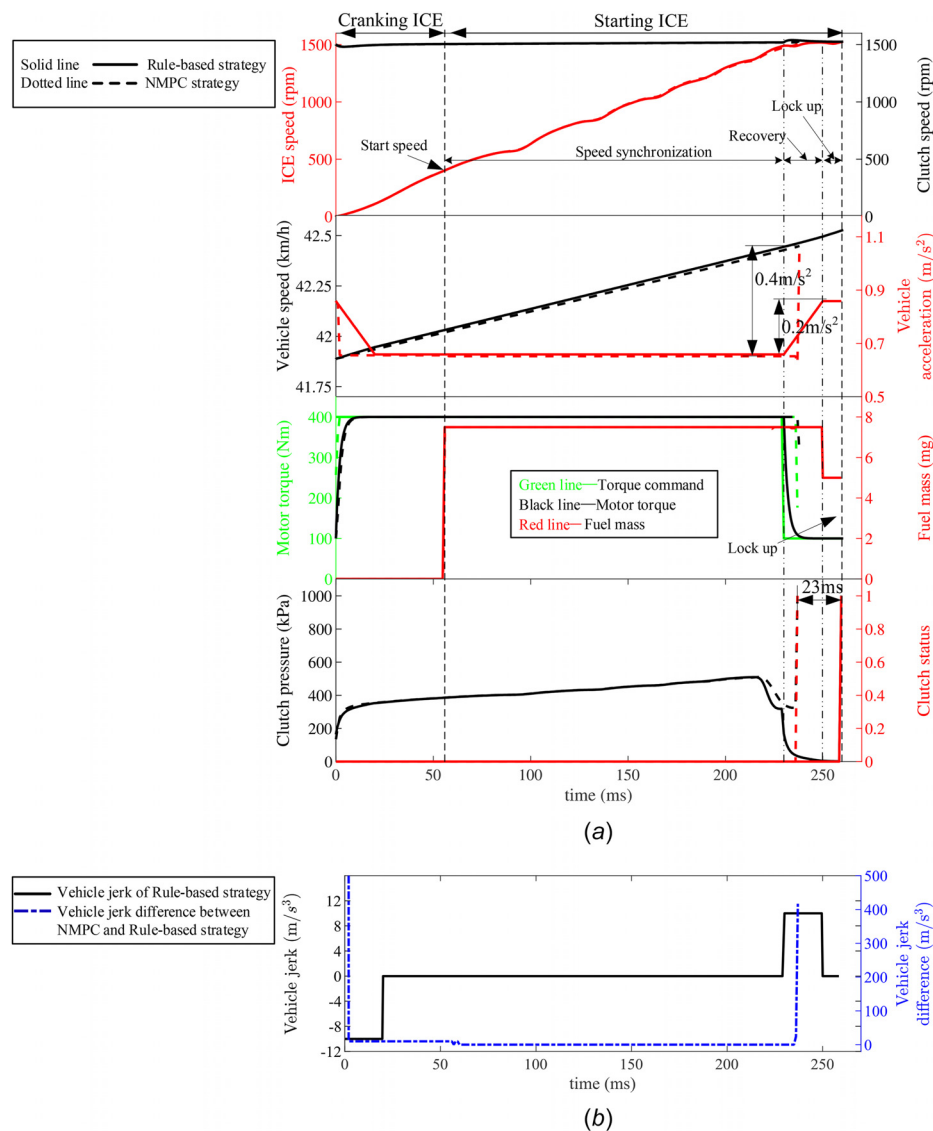

(a)

(b)

Fig. 19 Comparison between the rule-based control strategy and NMPC. (a) Trajectories of ICE speed, motor speed, vehicle speed, vehicle acceleration, motor torque, fuel mass, clutch pressure, and clutch status. (b) Trajectories of vehicle jerk of rule-based strategy and jerk difference between two strategies.

Table 3   Comparison table

Type	NMPC	Rule-based	Percent%
Cranking	55 ms	55 ms	
Speed synchronization	182 ms	175 ms	
Recovery	0 ms	20 ms	
Lock up	0 ms	10 ms	
Whole process	237 ms	260 ms	+9.7%
Peak to peak acceleration	0.4 m/s^2	0.2 m/s^2	−50%
Vehicle jerk	$\gg$ 10 m/s^3 ✗	$\leq$ 10 m/s^3 ✓	
Equivalent fuel cost over NEDC	3568.7 μL	3716.7 μL	+4.15%

By comparing the two strategies in Fig. 19, we can see the rule-based control strategy takes more time to finish the engine-start process but with less vehicle jerk. As shown in Fig. 19(a), recovery and lock-up stages take more time than NMPC. To recover to the original and lock up within an appropriate vehicle jerk, the rule-based control strategy took 23 ms more than that of NMPC strategy, but it has better drivability performance. The maximum peak-to-peak acceleration is 0.2 m/s^2 while 0.4 m/s^2 with NMPC. The vehicle jerk of the rule-based strategy and the jerk difference between the two strategies are shown in Fig. 19(b). The maximum vehicle jerk of the proposed strategy is 10 m/s^3, much lower than that of the NMPC. More specifics are shown in Table 3.

To evaluate the fuel consumption difference between the NMPC and rule-based strategy, we test them under the New European Driving Cycle (NEDC), shown in Fig. 20. The engine-start process occurs at the same moment [12]. The engine-start control

Fig. 21   Clutch pressure trajectory

(a)

(b)
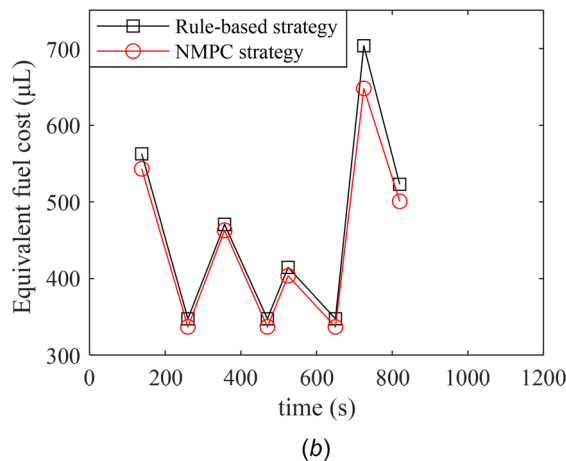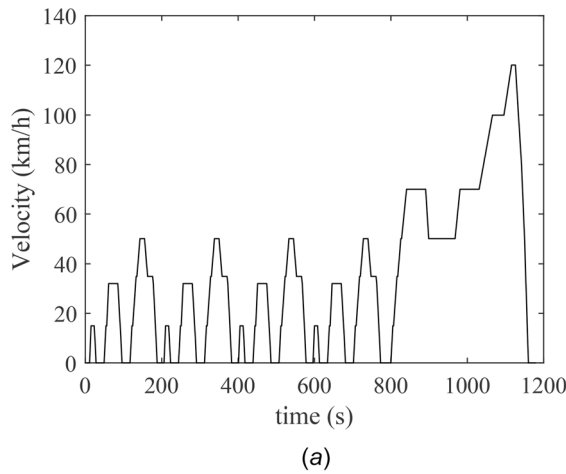
Fig. 20   Equivalent fuel cost comparison. (a) Driving cycle of NEDC. (b) Equivalent fuel cost.
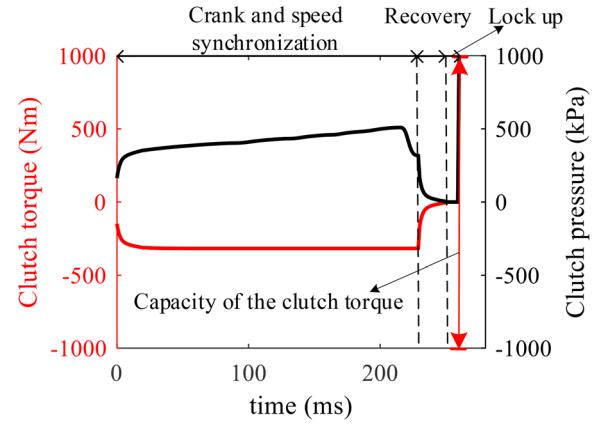
strategy is executed eight times in one cycle. The total fuel consumption for two strategies is 3568.7 μL and 3716.7 μL, respectively. The conversion factor between electricity and diesel fuel refers to the United States Environmental Protection Agency [39]. The rule-based control strategy takes about 4.15% more fuel than the NMPC. Moreover, the proposed control strategy takes 40 ms (13.3%) less than that with MPC in Ref. [18] although the belted starter alternator is utilized in Ref. [18]. The reason is that both the drive motor and the ICE are involved in the process herein.

During the whole process, the clutch behavior makes the vehicle obtain the designed acceleration, ensuring the vehicle jerk, which is analyzed next.

7.2   Clutch Behavior Analysis. Figure 21 depicts the clutch torque trajectory during the engine-start process. It can be seen that the clutch torque slowly increases at the beginning and then flattens with a relative high value. It can be described as follows:

$$T_{\text{clt\_}r} = J_2\dot{\omega}_3 + J_3\dot{\omega}_3 + \frac{T_{f\_\text{vel}}}{i_o} - T_{\text{motor}} \qquad (45)$$

where $T_{\text{motor}} = T_m^{\max}$.

Based on Eq. (45), it can be claimed that with the proposed control strategy, the ICE accelerates with maximum capacity of the motor through the clutch, which ensures the time optimality.

7.2.1   Analysis of Initial Clutch Torque. The initial clutch torque refers to the clutch torque at the beginning of the cranking process. A larger initial clutch torque means a higher possibility to decrease the engine-start time. We find that the parameters of the absorber, the motor torque response time (τ_m), and the declining time (τ_a) of the vehicle acceleration have influence on the initial clutch torque. According to Eq. (41), the initial clutch torque can be solved as follows:

$$T_{\text{clt\_}0} = (J_2 + J_3)\frac{a_{\text{vel}}}{r_{\text{vel}}}i_0 + \frac{T_{f\_\text{vel}}}{i_o} - T_{\text{motor}}$$
$$+ J_2\left(\frac{C_1 k_a + C_2 v_{\text{vel}} a_{\text{vel}} - \frac{\left(T_m^{\text{cmd}} - T_{\text{motor}}^0\right)}{\tau_m} - k_\theta \Delta\omega_{23\_0}}{k_\omega}\right)$$
$$\qquad (46)$$

where the first three items, $(J_2 + J_3)(a_{\text{vel}}/r_{\text{vel}})i_0 + (T_{f\_\text{vel}}/i_o) - T_{\text{motor}}$, indicate the clutch torque without the absorber. The remaining item, $J_2((C_1 k_a + C_2 v_{\text{vel}} a_{\text{vel}} - ((T_m^{\text{cmd}} - T_{\text{motor}}^0)/\tau_m) - k_\theta \Delta\omega_{23\_0})/k_\omega)$, reflects the effect of the absorber on the initial clutch torque.

Figure 22(a) shows the influence of the viscous coefficient and stiffness coefficient of the absorber on the initial clutch torque. As

(a)

(b)
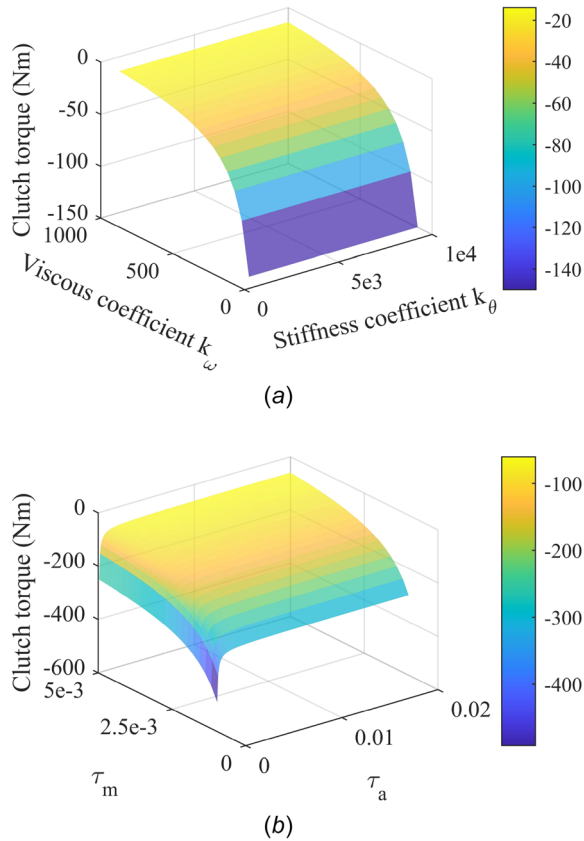
Fig. 22 Effect of parameters on the initial clutch torque. (a) Parameters of the absorber. (b) Parameters of the motor.

depicted, the initial clutch torque increases when the viscous coefficient decreases. This is expected, since when the viscous coefficient approaches infinity, it is similar to the situation without the absorber. The stiffness coefficient has no influence on the initial clutch torque because the absorber speed ($\Delta\omega_{23\_0}$) equals zero at the beginning. Therefore, with the absorber, the initial clutch torque could be nonzero or even larger.

Figure 22(b) illustrates the effect of time constants τ_a and τ_m on the initial clutch torque. The initial torque increases when the time constant τ_m decreases. That means if the motor responds faster, the initial clutch torque is larger. Moreover, the vehicle acceleration constant τ_a does not have much influence on the

Fig. 23 Absorber speed trajectory

initial clutch torque until τ_a is extremely small. A small vehicle acceleration constant τ_a means a large vehicle jerk, which should be prevented when designing the vehicle acceleration trajectory.

7.3 Analysis of Lock-Up Process. According to the analysis of the lock-up process in Sec. 6.2.2, the absorber speed influences the jerk during the lock-up process. This is shown in Fig. 23. As depicted, the absorber speed is small at the lock-up stage, and the vehicle jerk is also small with the proposed control strategy.

8 Conclusion

A dynamic model for the P2 powertrain system is constructed with the proposed Karnopp and Stribeck combined wet clutch model and a cylinder-by-cylinder diesel model in details. Based on the dynamic model, a rule-based control strategy including the ICE torque control for the engine-start process is derived from the results of NMPC. With both the drive motor and ICE involved in the process, it takes 260 ms to finish the process, 13.3% less time than that with MPC in the previous study [18]. The proposed rule-based control strategy takes about 4.15% more fuel than the NMPC over one cycle of NEDC. Moreover, with a predesigned vehicle acceleration trajectory, the control strategy ensures that the engine can start with the desired vehicle jerk $\leq 10\,\mathrm{m/s^3}$ and peak-to-peak vehicle acceleration $\leq 0.2\,\mathrm{m/s^2}$.

(1) With the proposed control strategy, the motor can perform at its maximum capacity to accelerate the engine-start process. Moreover, the vehicle acceleration can be designed to meet the requirements of the vehicle jerk. Finally, the proposed control strategy can accelerate the engine-start process with a low vehicle jerk, around 10 m/s³ herein.

(2) The initial clutch torque at the kissing point depends on the viscous coefficient of the absorber and the motor torque response ability. Larger initial clutch torque means greater potential of decreasing the engine-start time. With the absorber, the initial clutch torque can be nonzero or even larger. When the viscous coefficient of the absorber is lower, we can achieve a larger initial clutch torque. When the motor torque responds faster, the initial clutch torque can also be larger.

(3) The absorber speed has significant influence on the vehicle jerk. A smaller fluctuation of the absorber speed results in a smaller vehicle jerk.

The proposed control strategy can be used in the feedforward control fashion as a reference signal generator.

Acknowledgment

References

[1] Chan, C. C., Bouscayrol, A., and Chen, K., 2010, "Electric, Hybrid, and Fuel-Cell Vehicles: Architectures and Modeling," IEEE Trans. Veh. Technol., **59**(2), pp. 589–598.
[2] Hackmann, W., Wagner, B., Zwingel, R., Dziedzek, I., and Welke, K., 2007, "Fremderregte Synchronmaschinen im Einsatz Als Achshybridantriebe," *International ETG Congress*, Karlsruhe, Germany, Oct. 23–24, pp. 55–64.
[3] Smith, A., Bucknor, N., Yang, H., and He, Y., 2011, "Controls Development for Clutch-Assisted Engine Starts in a Parallel Hybrid Electric Vehicle," SAE Paper No. 2011-01-0870.
[4] Song, M., Oh, J., Choi, S., Kim, Y., and Kim, H., 2013, "Motor Control of a Parallel Hybrid Electric Vehicle During Mode Change Without an Integrated Starter Generator," J. Electr. Eng. Technol., **8**(4), pp. 930–937.
[5] Kum, D., Peng, H., and Bucknor, N. K., 2013, "Control of Engine-Starts for Optimal Drivability of Parallel Hybrid Electric Vehicles," ASME J. Dyn. Syst., Meas., Control, **135**(2), p. 021020.
[6] Chen, L., Xi, G., and Sun, J., 2012, "Torque Coordination Control During Mode Transition for a Series–Parallel Hybrid Electric Vehicle," IEEE Trans. Veh. Technol., **61**(7), pp. 2936–2949.
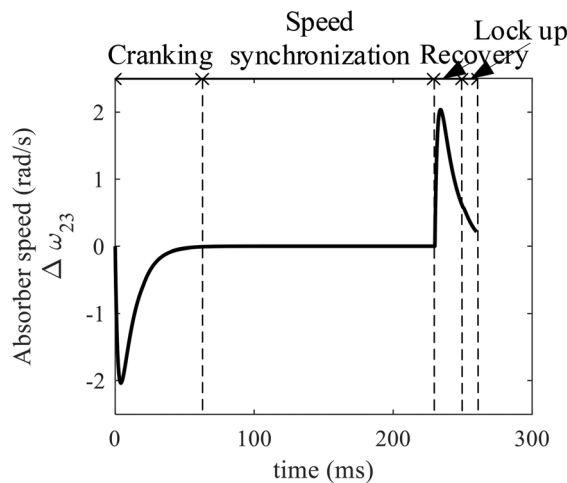
[7] Lei, Z., Sun, D., Liu, Y., Qin, D., Zhang, Y., Yang, Y., and Chen, L., 2017, "Analysis and Coordinated Control of Mode Transition and Shifting for a Full Hybrid Electric Vehicle Based on Dual Clutch Transmissions," Mech. Mach. Theory, 114, pp. 125–140.

[8] Xu, X., Wu, X., Jordan, M., Dong, P., and Liu, Y., 2018, "Coordinated Engine-Start Control of Single-Motor P2 Hybrid Electric Vehicles With Respect to Different Driving Situations," Energies, 11(1), p. 207.

[9] Dong, P., Wu, S., Guo, W., Xu, X., Wang, S., and Liu, Y., 2020, "Coordinated Clutch Slip Control for the Engine Start of Vehicles With P2-Hybrid Automatic Transmissions," Mech. Mach. Theory, 153(3), p. 103899.

[10] Ning, J., Zhu, G., and Qu, B., 2018, "Development of a Engine Start Control Method for P2 Hybrid Vehicles in Launch Situation," IFAC-PapersOnLine, 51(31), pp. 7–10.

[11] Zhao, C., Zu, B., Xu, Y., Wang, Z., and Zhao, G., 2019, "Analysis of a Coordinated Engine-Start Control Strategy for P2 Hybrid Electric Vehicle," SAE Paper No. 2019-01-5023.

[12] Zhao, C., Zu, B., Xu, Y., Wang, Z., Zhou, J., and Liu, L., 2020, "Design and Analysis of an Engine-Start Control Strategy for a Single-Shaft Parallel Hybrid Electric Vehicle," Energy, 202, p. 117621.

[13] Cvok, I., Ranogajec, V., Deur, J., Zhang, Y., Ivanovic, V., and Fujii, Y., 2022, "Analysis of Improving Automatic Transmission Upshift Performance by Using Off-Going Clutch During Inertia Phase," ASME J. Dyn. Syst., Meas., Control, 144(2), p. 021005.

[14] Sun, G., Sun, D., Ma, K., Kan, Y., and Shi, J., 2022, "Analysis and Control of Engine Starting Process Based on a Novel Single-Motor Power-Reflux Hybrid Electric Vehicle," Mech. Mach. Theory, 168, p. 104616.

[15] Beck, R., Richert, F., Bollig, A., Abel, D., and Noreikat, K. E., 2005, "Model Predictive Control of a Parallel Hybrid Vehicle Drivetrain," IEEE Conference on Decision and Control European Control Conference (CDC-ECC), Seville, Spain, Dec. 15, pp. 2670–2675.

[16] Dudek, R., Smidl, V., and Peroutka, Z., Start-Stop System for a City Bus Based on Model Predictive Control, IECON 2014-40th Annual Conference of the IEEE Industrial Electronics Society, IEEE, Dallas, TX.

[17] Stroe, N., Olaru, S., Colin, G., Ben-Cherif, K., and Chamaillard, Y., 2018, "Time-Varying MPC-Based Energy Management for HEV Including Engine Stop & Start," International Conference on System Theory, Sinaia, Romania, Oct. 13–15, pp. 790–795.

[18] Han, Z., Hu, Y., Sun, P., and Hong, C., 2017, "Model Predictive Control of Diesel Engine Start-Stop Control in an HEV," 36th Chinese Control Conference (CCC), Dalian, China, July 26–28, pp. 9590–9595.

[19] Wang, D., Hu, M., Li, B., Qin, D., and Sun, D., 2020, "Study on the Influence Factors Upon the Propensity to Stick-Slip Phenomenon During Vehicle Start-Up Process," IEEE Access, 8(99), pp. 12343–12353.

[20] He, Y., Bucknor, N. K., Smith, A. L., and Yang, H., 2010, "Modeling and Drivability Assessment of a Single-Motor Strong Hybrid at Engine Start," SAE Paper No. 2010-01-1440.

[21] Shin, C., Choi, J., Cha, S., and Lim, W., 2014, "An Objective Method of Driveability Evaluation Using a Simulation Model for Hybrid Electric Vehicles," Int. J. Precis. Eng. Manuf., 15(2), pp. 219–226.

[22] Sim, K., Oh, S.-M., Namkoong, C., Lee, J.-S., Han, K.-S., and Hwang, S.-H., 2017, "Control Strategy for Clutch Engagement During Mode Change of Plug-In Hybrid Electric Vehicle," Int. J. Automot. Technol., 18(5), pp. 901–909.

[23] Huang, W., Liu, H. J., and Ma, Y. F., 2019, "Drivability Evaluation Model Using Principal Component Analysis and Optimized Extreme Learning Machine," J. Vib. Control, 25(16), pp. 2274–2281.

[24] Karlsson, J., and Fredriksson, J., 1999, "Cylinder-by-Cylinder Engine Models versus Mean Value Engine Models for Use in Powertrain Control Applications," SAE Paper No. 1999-01-0906.

[25] Karnopp, D., 1985, "Computer Simulation of Stick-Slip Friction in Mechanical Dynamic Systems," ASME J. Dyn. Syst., Meas., Control, 107(1), pp. 100–103.

[26] Stribeck, R., 1903, Wesentliche Eigenschaften der Gleit-und Rollenlager, Springer, pp. 1341–1348, 1432–1438 and 1463–1470.

[27] Andersson, S., Söderberg, A., and Björklund, S., 2007, "Friction Models for Sliding Dry, Boundary and Mixed Lubricated Contacts," Tribol. Int., 40(4), pp. 580–587.

[28] Bianchi, D., Rolando, L., Serrao, L., Onori, S., Rizzoni, G., Khayat, N. A., Hsieh, T. M., and Kang, P., 2011, "Layered Control Strategies for Hybrid Electric Vehicles Based on Optimal Control," Int. J. Electr. Hybrid Veh., 3(2), pp. 191–217.

[29] Biasini, R., Onori, S., and Rizzoni, G., 2013, "A near-Optimal Rule-Based Energy Management Strategy for Medium Duty Hybrid Truck," Int. J. Powertrains, 2(2/3), pp. 232–261.

[30] Ramste30dt, M., 2004, "Cylinder-by-Cylinder Diesel Engine Modelling: A Torque-Based Approach," Master's thesis, Department of Electrical Engineering, Linkoping University, Linköping, Sweden.

[31] Hashemzadeh Nayeri, M., 2005, "Cylinder-by-Cylinder Torque Model of an SI-Engine for Real-Time Applications," Master's thesis, Department of Electrical Engineering, Linkoping University, Linköping, Sweden.

[32] Kiencke, U., and Nielsen, L., 2000, Automotive Control Systems: For Engine, Driveline, and Vehicle, Springer Berlin, Heidelberg/New York.

[33] Romano, R. A., and Garcia, C., 2008, "Karnopp Friction Model Identification for a Real Control Valve," IFAC Proc. Vol., 41(2), pp. 14906–14911.

[34] Aberger, M., and Otter, M., 2002, "Modeling Friction in Modelica With the Lund-Grenoble Friction Model," Proceedings of 2nd International Modelica Conference, Oberpfaffenhofen, Mar. 18–19, pp. 285–294. Modelica 2002, Mar. 18–19, Oberpfaffenhofen.

[35] Berger, E. J., 2002, "Friction Modeling for Dynamic System Simulation," ASME Appl. Mech. Rev., 55(6), pp. 535–577.

[36] Sim, K., Oh, S.-M., Kang, K.-Y., and Hwang, S.-H., 2017, "A Control Strategy for Mode Transition With Gear Shifting in a Plug-In Hybrid Electric Vehicle," Energies, 10(7), p. 1043.

[37] Mathworks, 2021, "nlmpc," Mathworks, Natick, MA, 2021, accessed Nov. 11, 2022, https://ww2.mathworks.cn/help/mpc/ref/nlmpc.html

[38] Nocedal, J., and Wright, S., 2006, Numerical Optimization, Springer Science & Business Media, New York.

[39] Khajepour, A., Fallah, M. S., and Goodarzi, A., 2014, "Electric and Hybrid Vehicles," Int. J. Veh. Des., 200(152) pp. 2/1–2/4.